

光学学报

基于卷积神经网络和多孔干涉仪的分数完美涡旋光束轨道角动量的识别

杜浩波, 陈君*, 傅钢坤, 李岩松, 王海龙, 石岩, 赵春柳, 金尚忠**

中国计量大学光学与电子科技学院, 浙江杭州 310018

摘要 完美涡旋光束(POVB)的光斑不随拓扑荷的变化而变化, 在微粒操控、光通信、激光材料处理等领域具有广泛应用。POVB的准确识别具有重要的研究意义。提出一种卷积神经网络结合多孔干涉仪的方法来识别0.01阶分数POVB。实验结果表明, 在理想环境下, 0.01阶分数POVB的识别率达到100%。在扇形遮挡90°和扇形遮挡180°情况下, 0.01阶分数POVB的识别率分别达到100%和99.5%。本研究为识别0.01阶分数POVB提供了一种新的方法, 对于该光束的应用和推广具有重要意义。

关键词 物理光学; 卷积神经网络; 多孔干涉仪; 分数完美涡旋光束; 轨道角动量; 拓扑荷

中图分类号 TN247

文献标志码 A

DOI: 10.3788/AOS221459

1 引言

具有轨道角动量(OAM)模式的涡旋光束具有螺旋相位波前, 表示为 $\exp(il\varphi)$, 其中 φ 表示方位角, l 表示拓扑荷(TC)^[1-2]。涡旋光束具有OAM, 受到了科学家们的广泛关注, 研究人员对其在微粒操控^[3]、量子成像^[4]、光通信^[5-7]、遥感^[8]等领域中的应用进行了研究。然而, 涡旋光束的半径依赖于TC数, 其中心亮环半径会随着TC值的增大而增大^[9], 这使得具有较大TC值的涡旋光束在传输、耦合等场合中的应用变得非常困难^[10-12]。为了克服传统涡旋光束这一缺点, 2013年, Ostrovsky等^[13]提出半径不随TC值的增大而改变的新型光束, 并称之为完美涡旋光束(POVB)。随后, 人们从实验上实现了POVB, 并扩展了此类光束的应用^[14-20]。POVB因其半径不随TC的改变而变化, 在微粒操控^[21]、光通信^[22]领域中具有巨大的应用前景。与整数阶的POVB相比, 分数阶POVB的环形强度分布具有径向开口的特性, 其在微粒操控^[23]、聚焦成形^[24]等方面具有优势。此外, 在光通信领域中, 分数阶的POVB可以表征更丰富的信息量, 具有更大的通信容量^[25]。实现以上应用的前提是对分数阶POVB的TC的正确判断。只有实现高精度POVB识别才能进行精准的微粒操控和实现高质量的结构光信息传输。因此提高POVB的识别精度就变得尤为重要。

2017年, Ma等^[26]通过相移技术让POVB与其共

轭光束精确地重叠和干涉, 最后通过计算干涉条纹的数量来确定POVB的TC。该方法可以在不需要额外光学元件的情况下原位测定POVB的TC, 并且不受环境振动和寄生干扰^[27]的影响。采用模态分解法^[28]对POVB的TC进行定量测量时具有较高的能量效率, 但是该方法仅适用于傅里叶平面, 并且只能测量整数阶TC。一种测量任意阶POVB的TC的方法^[29]在2021年被报道, 通过动态角度双缝法(ADS)实现了对任意POVB的TCs的精准测量, 该方法将POVB转换为ADS角平分方向上的干涉强度图, 并从周期性变化的干涉图中获取TC的信息, 理论值与拟合结果的偏差小于2%, 说明该检测方法是有效、合理的。但是现有方法仍面临非理想环境下分数阶POVB识别的问题。

卷积神经网络作为深度学习的一种重要技术, 不仅在图像处理、自然语言处理等方面展现了巨大的优势, 也为OAM领域的研究做出了巨大贡献^[30-31]。由于POVB半径一致, 直接使用卷积神经网络对分数POVB分类的效果并不理想。基于此, 本文采用卷积神经网络和多孔干涉仪(MI)相结合的方法对分数POVB进行识别。POVB经过MI后产生不同的光斑, 形成的光斑结构与TC信息是一对一的关系, 这解决了POVB空心光斑半径相同导致的卷积神经网络识别TC准确率低的问题。实验结果表明, 本文方法在理想环境下能识别0.01阶分数POVB, 识别率高达

收稿日期: 2022-07-11; 修回日期: 2022-08-09; 录用日期: 2022-09-06; 网络首发日期: 2022-09-16

基金项目: 浙江省重点研发计划项目(2021C01068)、浙江省之江实验室重大科研项目(2019DE0KF01)

通信作者: *chenjun.sun@cjlu.edu.cn; **jinsz@cjlu.edu.cn

100%。在扇形遮挡90°和扇形遮挡180°的非理想环境下,本文方法依旧能识别0.01阶分数POVB,识别率分别达到100%和99.5%。

2 理 论

2.1 完美涡旋光束与多孔干涉仪

理论上,POVB的产生可以通过对贝塞尔-高斯(BG)光束^[18]进行傅里叶变换来实现。在极坐标(r, ϕ)中,BG光束的复场振幅为

$$E(r, \phi) = J_l(k_r r) \exp(il\phi) \exp\left(-\frac{r^2}{w_g^2}\right), \quad (1)$$

式中: J_l 是第一类 l 阶贝塞尔函数; ϕ 为方位角; k_r 为径向波数; w_g 为高斯光束的束腰宽度。BG光束通过焦距为 f 的傅里叶透镜后在焦平面上形成POVB,其数学描述如下:

$$E(r, \phi) = i^{l-1} \frac{w_g}{w_0} \exp(il\phi) \exp\left[-\frac{(r-r_r)^2}{w_0^2}\right], \quad (2)$$

式中: r_r 是POVB的半径; $w_0 = 2f/(k w_g)$ 是傅里叶变换透镜焦面处高斯光束的束腰。POVB经过MI后产

生的复振幅^[32]可表示为

$$o(x, y) = \sum_{n=1}^N \text{circ}\left[\frac{\sqrt{(x-x_n)^2 + (y-y_n)^2}}{r_0}\right] E(r, \phi), \quad (3)$$

式中:circ(•)为圆孔的透过率函数;(x_n, y_n)为圆孔中心的坐标; r_0 为小孔的半径; N 为MI的孔数。在夫琅禾费极限下,经MI的POVB在探测平面形成多孔干涉图案,其强度分布为

$$I \propto |\mathcal{F}[o(x, y)]|^2, \quad (4)$$

式中: $\mathcal{F}[\cdot]$ 表示傅里叶变换。合适的MI的孔径数 N 可使POVB产生与TC一一对应的多孔干涉图案,达到通过识别多孔干涉图案来识别分数阶POVB拓扑荷的目的。POVB在不同孔径数 N 下产生不同的干涉图案,但干涉图案与光束TC的关系仍然满足一一对应的关系,因此神经网络依旧能识别不同孔数的干涉图样。本文讨论的非理想环境包括90°的扇形遮挡和180°的扇形遮挡。如图1所示,扇形遮挡固定在同一位置。这两种扇形遮挡将会产生振幅干扰。

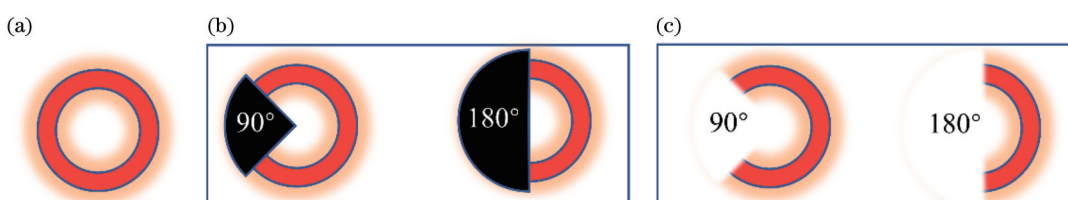


图1 扇形遮挡示意图(黑色扇形为不透光障碍物)。(a)未经历障碍物的光束光斑;(b)障碍物的位置;(c)与障碍物作用后的光束光斑

Fig. 1 Schematic diagrams of sector-shaped opaque obstacle (black sectors are opaque obstacles). (a) Beam spot without passing through obstacles; (b) location of obstacles; (c) beam spots after interaction with obstacles

图2为理论模拟的POVB经过MI后的干涉图像。本文考虑了理想环境(简写为Ide)下和非理想环境(简写为N-Ide)下的MI干涉图像。从图2(a)中可以看出POVB经过MI后的干涉光斑花纹随TC的数值变化

而发生改变,其原因是POVB经过MI后局部相位发生改变,产生了不同的干涉图案。这使得探测面处的光斑图案与待测光束的初始TC数存在一一对应的关系。图2(a)中0.01阶分数POVB经过MI后的图案随

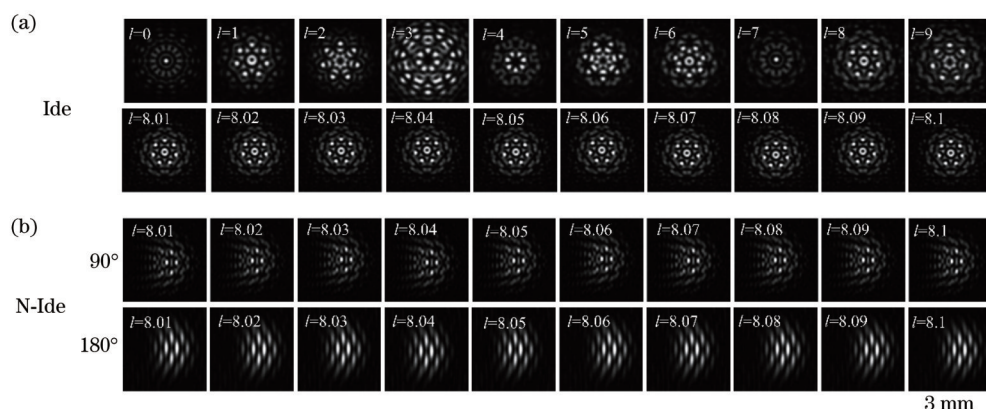


图2 理论模拟的不同TC的POVB经过MI后的干涉图案(l 代表TC数值)。(a)理想环境;(b)非理想环境

Fig. 2 Interference patterns of POVB with different TC after MI obtained by theoretical simulation (l represents TC value). (a) Ide; (b) N-Ide

TC的变化而变化,但人眼无法将其分辨出。图2(b)的图案是考虑了非理想因素,分别是图1中的 90° 和 180° 扇形遮挡,可以看出随着遮挡角度的增大,图案特征将会减少,识别的难度增大。

2.2 网络结构

针对0.01阶分数POVB的TC识别问题,设计了一个6层的卷积神经网络来对分数POVB的干涉图像进行分类。网络结构如图3所示。首先将采集的光强图像从 $640\text{ pixel} \times 480\text{ pixel}$ 的图像转化成 $224\text{ pixel} \times 224\text{ pixel}$ 的图像,作为网络结构的输入数据。图像经过第一个卷积块,其包含了32个 5×5 的卷积核、1个BN层、1个ReLU激活函数和1个 2×2 的最大池化

层。干涉图像从输入到输出一共经过4个卷积块和2个全连接层。第2个卷积块与第1个卷积块相同。第3个和第4个卷积块是由64个 5×5 的卷积核和1个 2×2 的最大池化层组成。最后2层是1个神经元个数为128和1个神经元个数为10的全连接层。最后1个全连接层中的神经元与softmax激活函数相连。卷积核的作用是对图像进行特征提取,并减少模型训练的参数。BN层的作用是加快网络训练和收敛的速度。ReLU激活函数同样也起到了缓解过拟合的问题。最大池化层的作用是对特征进行压缩。相比于经典的Densenet网络,这个模型仅有6层。相同情况下,该模型所用的训练时间更短。

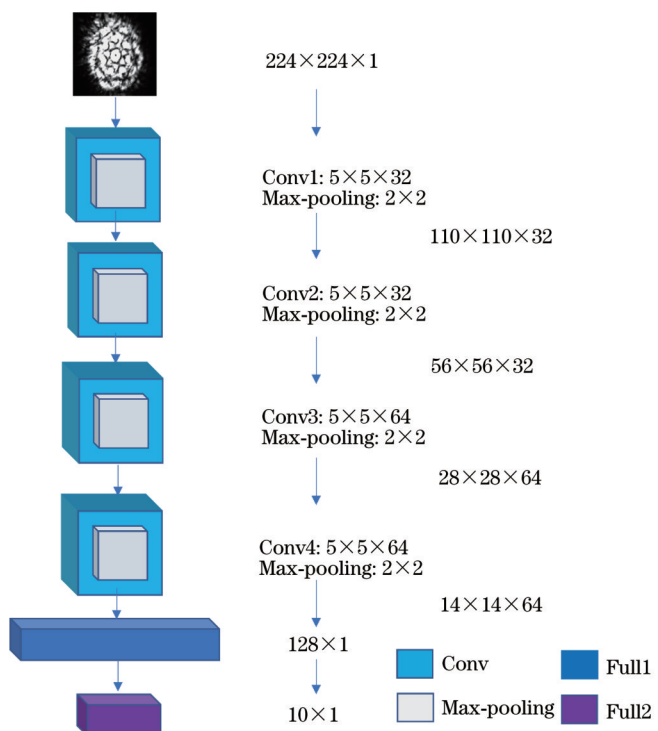


图3 本实验的网络结构

Fig. 3 Network structure of experiment

3 实验

3.1 实验装置

实验装置如图4所示。氦氖激光器产生一个稳定的高斯光束,其波长为633 nm。在实验中,空间光调制器(SLM)是一个纯相位反射液晶器件,其分辨率为 $1280\text{ pixel} \times 720\text{ pixel}$,像素尺寸为 $6.3\text{ }\mu\text{m}$,工作频率为50 Hz。MI是通过在SLM上加载计算全息图(CGH)产生。透镜焦距 $f_1=35\text{ cm}$,CCD相机为工业相机,分辨率为 $640\text{ pixel} \times 480\text{ pixel}$,相机帧率为125 frame/s。SLM到光阑的距离为22 cm,光阑到透镜的距离为8 cm。光阑、透镜和SLM的位置固定,CCD到透镜的距离为 $z=10\text{ cm}$, z 可根据实验需求进行调节。

3.2 训练及结果分析

实验中,在SLM上加载计算全息图,产生BG光束^[17]。POVB实验参数设置: $w_0=31.5\text{ }\mu\text{m}$, $w_g=157.5\text{ }\mu\text{m}$, $k_r=0.06\text{ }\mu\text{m}^{-1}$ 。BG光从SLM出射并传输一定距离,达到远场条件,在夫琅禾费平面转变成POVB光。POVB的多孔干涉图案是通过在SLM上加载POVB和MI透过率函数来实现的。POVB的多孔干涉图案的实验参数设置为 $r_r=267.8\text{ }\mu\text{m}$ 。从实验中发现:当 $N \leq 2$ 时,干涉图案与TC的对应关系不能形成,此时,神经网络无法进行准确的TC识别;当N大于17时,受SLM分辨率的影响,本实验的孔径模拟失真,干涉图像与TC的对应关系也不能形成。因此,在本实验中,N的范围应为3~16。本实验中MI所选取的孔数为 $N=7$,MI的孔半径 $r_0=0.25\text{ mm}$ 。图5(a)中POVB指POVB在探测面的实验

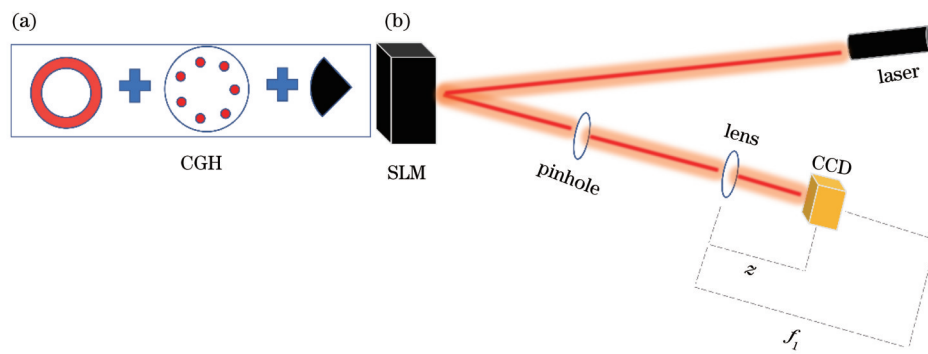


图4 本实验示意图。(a)在角向障碍物遮挡下的多孔板示意图(多孔板的透过率函数由CGH来实现);(b)实验光路图

Fig. 4 Schematic diagrams of experiment. (a) Schematic diagram of multi-aperture plate under angular obstacles (transmittance function of multi-aperture plate is realized by CGH); (b) schematic diagram of experimental setup

光斑。由于POVB的光斑半径不随TC的数值改变而变化,直接使用基于光斑的深度学习方法进行识别,误差较大。**图5**中POVB+MI指POVB经过MI后在探测面的多孔干涉图案。从实验结果可见,**图5(a)**中

POVB经过MI后光斑图案与TC具有一对一的关系,这与理论仿真的结果吻合。对于0.01阶分数POVB与TC的对应关系,人眼无法分辨,如**图5(b)**所示,此时需要用深度学习的方法对其进行分辨。

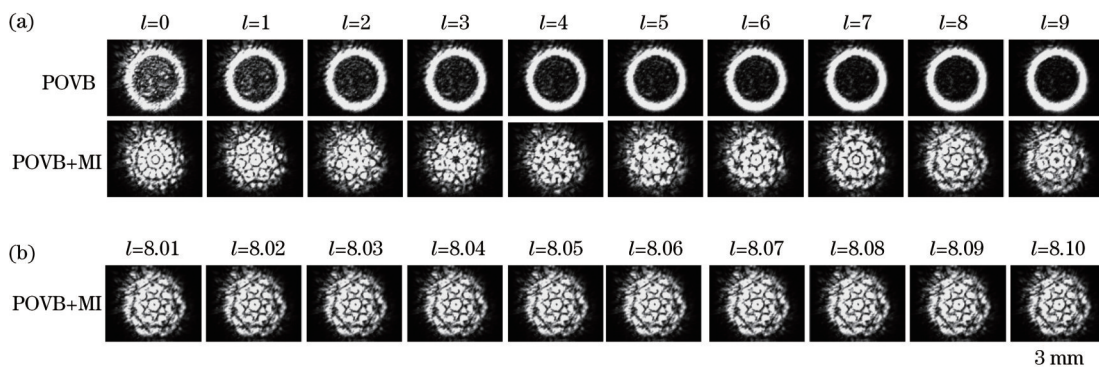


图5 实验获得的POVB光斑和经过MI干涉的光斑。(a)理想环境下 $l=0, 1, \dots, 9$ 的POVB图案和POVB+MI图案;(b)理想环境下 $l=8.01, 8.02, \dots, 8.10$ 的POVB+MI图案

Fig. 5 Experimental results of spots of POVB before and after MI. (a) Patterns of POVB and POVB+MI with $l=0, 1, \dots, 9$ under ideal environment; (b) patterns of POVB+MI with $l=8.01, 8.02, \dots, 8.10$ under ideal environment

实验中收集拓扑荷 l 为8.01~8.10的多孔干涉图作为训练数据。每一个TC收集400张图像,总共4000张图像作为数据集。**图5(b)**是干涉光强图,其中 l 为8.01的图案所对应的标签为0, l 为8.02的图案所

对应的标签为1,以此类推, l 为8.10所对应的标签为9。将数据集按照7:2:1划分为训练集、验证集和测试集,将训练集和验证集放进本实验设计的模型进行训练。训练结果如**图6(a)**所示:实线代表的是训练集准

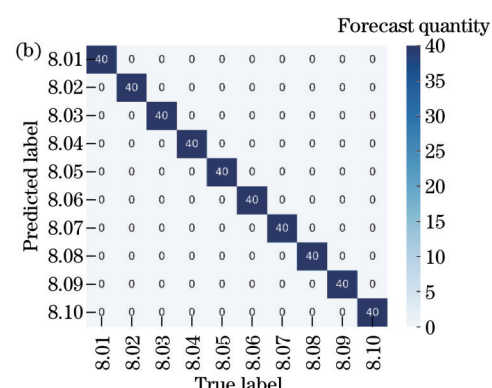
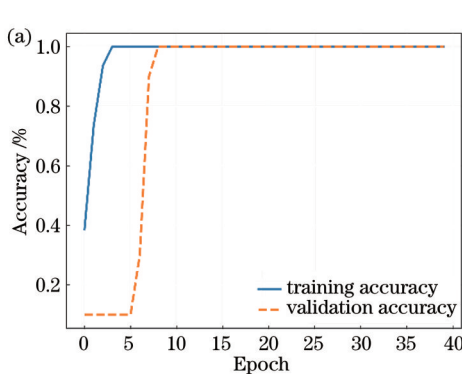


图6 0.01阶分数POVB+MI的光斑训练结果与混淆矩阵。(a)理想环境下的0.01阶分数POVB+MI的光斑训练结果;(b)分数阶POVB+MI的混淆矩阵

Fig. 6 Training results and confusion matrix of 0.01 order fractional POVB+MI. (a) Training results of 0.01 order fractional POVB+MI under ideal environment; (b) confusion matrix of fractional POVB+MI

确率, 经过 3 个 epoch, 训练集准确率为 100%; 虚线代表的是验证集准确率, 经过 8 个 epoch, 验证集准确率为 100%。图 6(b)是测试分类的混淆矩阵, 可以看出, 该混淆矩阵的测试准确率为 100%。这说明本文方法对于 0.01 阶分数 POVB 的分类是高效且准确的, 也体现了深度学习在图像分类中的有效性。

为了模拟非理想环境下 0.01 阶分数 POVB 的光斑情况, 本实验在 SLM 加载的 CGH 上设置扇形遮挡。图 7 是 0.01 阶分数 POVB 的光斑图案和分数 POVB+MI 干涉图案。为了识别在遮挡环境下的 0.01 阶分数 POVB, 采用本文提出的卷积神经网络和

MI 相结合的方法。本实验在 90° 遮挡和 180° 遮挡下分别收集 4000 张 0.01 阶分数 POVB 的多孔干涉图像作为数据集。该数据集是由 10 个不同的 TC 标记, 按照 7:2:1 划分为训练集、验证集和测试集, 然后放进模型进行训练。

图 8(a)是在 90° 扇形遮挡下分数 POVB 经过 MI 的多孔干涉图像的训练结果图。实线为训练集的准确率, 可以看出经过 3 个 epoch 后, 训练集准确率为 100%。虚线是验证集的准确率, 可以看出经过 8 个 epoch 后, 验证集准确率达到 100%。为了检验训练之后模型的鲁棒性, 这里将分配好的测试集放进模型进

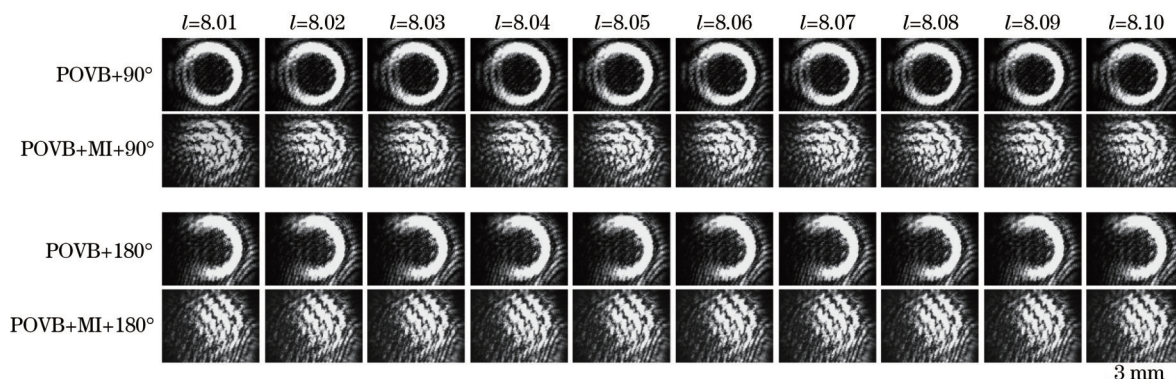


图 7 实验获得的非理想环境下 0.01 阶分数 POVB 的光斑和经过 MI 后的干涉图案(90° 和 180° 分别代表非理想环境下扇形遮挡的度数)
Fig. 7 Experimental patterns of 0.01 order fractional POVB before and after MI under non-ideal environment (90° and 180° represent degrees of sector-shaped opaque obstacle under non-ideal environment)

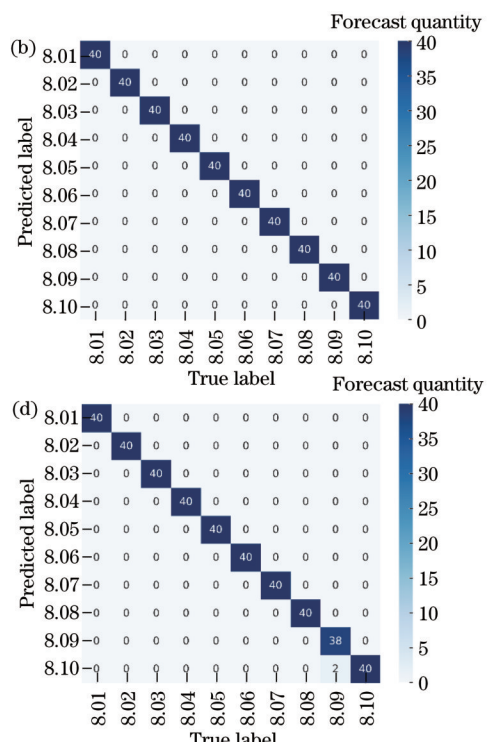
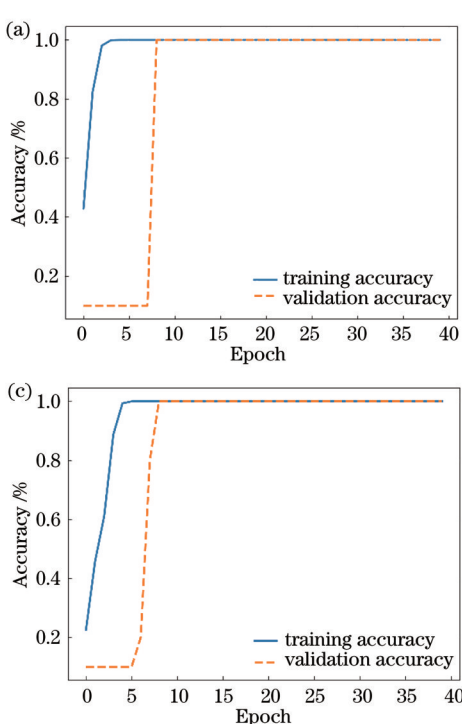


图 8 POVB+MI 在 90° 和 180° 扇形遮挡下的训练结果和混淆矩阵。(a) 90° 和 (c) 180° 扇形遮挡的 POVB+MI 的训练结果; (b) 90° 和 (d) 180° 扇形遮挡的混淆矩阵

Fig. 8 Training results and confusion matrices of POVB+MI under sector-shaped opaque obstacle with 90° and 180°. Training results of POVB+MI with (a) 90° and (c) 180° sector-shaped opaque obstacle, respectively; confusion matrices with (b) 90° and (d) 180° sector-shaped opaque obstacle, respectively

行测试,结果如图8(b)所示。从图8(b)中可以看出测试准确率为100%。结果表明,POVB经过MI后,在90°扇形遮挡环境下依旧能准确识别0.01阶分数POVB。图8(c)是在180°扇形遮挡下分数POVB经过MI的多孔干涉图像的训练结果图。实线为训练集的准确率,可以看出经过5个epoch后,训练集准确率为100%。虚线是验证集的准确率,可以看出经过8个epoch后,验证集准确率达到100%。图8(d)是该模型训练后测试集的混淆矩阵,可以看出该模型的测试准确率为99.5%。结果表明,在非理想环境下,本文提出的基于卷积神经网络和MI的方法依旧能识别0.01阶分数POVB。

4 结 论

提出卷积神经网络结合MI的方法,对理想环境和非理想环境下0.01阶分数POVB进行准确分类。本文方法基于TC对POVB相位的影响,使用MI产生具有TC特异性的POVB多孔干涉图案,然后利用卷积神经网络实现对0.01阶分数POVB的准确分类。实验结果表明,在理想环境下,本文方法对0.01阶分数POVB的识别率达到100%。对于90°和180°扇形遮挡的非理想环境,本文方法对0.01阶分数POVB的识别率分别为100%和99.5%。本文提出的方法为分数POVB的识别提供了一种新的方案。该研究显示了卷积神经网络和MI在分数涡旋光通信领域中的应用潜力。

参 考 文 献

- [1] Allen L, Beijersbergen M W, Spreeuw R J, et al. Orbital angular momentum of light and the transformation of Laguerre-Gaussian laser modes[J]. Physical Review A, 1992, 45(11): 8185-8189.
- [2] Padgett M J. Orbital angular momentum 25 years on[J]. Optics Express, 2017, 25(10): 11265-11274.
- [3] Ng J, Lin Z F, Chan C T. Theory of optical trapping by an optical vortex beam[J]. Physical Review Letters, 2010, 104(10): 103601.
- [4] Chen L X, Lei J J, Romero J. Quantum digital spiral imaging[J]. Light: Science & Applications, 2014, 3(3): e153.
- [5] Wang J. Advances in communications using optical vortices[J]. Photonics Research, 2016, 4(5): 14-28.
- [6] Willner A E. Vector-mode multiplexing brings an additional approach for capacity growth in optical fibers[J]. Light: Science & Applications, 2018, 7(3): 18002.
- [7] 马志远,陈康,张明明,等.拉盖尔-高斯幂指数相位涡旋光束传输特性[J].光学学报,2022,42(5):0526001.
Ma Z Y, Chen K, Zhang M M, et al. Propagation characteristics of Laguerre-Gaussian power-exponent-phase-vortex beams[J]. Acta Optica Sinica, 2022, 42(5): 0526001.
- [8] Xie G D, Song H Q, Zhao Z, et al. Using a complex optical orbital-angular-momentum spectrum to measure object parameters[J]. Optics Letters, 2017, 42(21): 4482-4485.
- [9] Zheng S, Wang J. Measuring orbital angular momentum (OAM) states of vortex beams with annular gratings[J]. Scientific Reports, 2017, 7: 40781.
- [10] Yan H W, Zhang E T, Zhao B Y, et al. Free-space propagation of guided optical vortices excited in an annular core fiber[J]. Optics Express, 2012, 20(16): 17904-17915.
- [11] Li S H, Wang J. Multi-orbital-angular-momentum multi-ring fiber for high-density space-division multiplexing[J]. IEEE Photonics Journal, 2013, 5(5): 7101007.
- [12] Brunet C, Vaity P, Messadeq Y, et al. Design, fabrication and validation of an OAM fiber supporting 36 states[J]. Optics Express, 2014, 22(21): 26117-26127.
- [13] Ostrovsky A S, Rickenstorff-Parrao C, Arrizón V. Generation of the “perfect” optical vortex using a liquid-crystal spatial light modulator[J]. Optics Letters, 2013, 38(4): 534-536.
- [14] Chen M Z, Mazilu M, Arita Y, et al. Dynamics of microparticles trapped in a perfect vortex beam[J]. Optics Letters, 2013, 38(22): 4919-4922.
- [15] García-García J, Rickenstorff-Parrao C, Ramos-García R, et al. Simple technique for generating the perfect optical vortex[J]. Optics Letters, 2014, 39(18): 5305-5308.
- [16] Chen Y, Fang Z X, Ren Y X, et al. Generation and characterization of a perfect vortex beam with a large topological charge through a digital micromirror device[J]. Applied Optics, 2015, 54(27): 8030-8035.
- [17] Chen M Z, Mazilu M, Arita Y, et al. Creating and probing of a perfect vortex *in situ* with an optically trapped particle[J]. Optical Review, 2015, 22(1): 162-165.
- [18] Vaity P, Rusch L. Perfect vortex beam: Fourier transformation of a Bessel beam[J]. Optics Letters, 2015, 40(4): 597-600.
- [19] Chaitanya N A, Jabir M V, Samanta G K. Efficient nonlinear generation of high power, higher order, ultrafast “perfect” vortices in green[J]. Optics Letters, 2016, 41(7): 1348-1351.
- [20] Li P, Zhang Y, Liu S, et al. Generation of perfect vectorial vortex beams[J]. Optics Letters, 2016, 41(10): 2205-2208.
- [21] Yan Y, Yue Y, Huang H, et al. Efficient generation and multiplexing of optical orbital angular momentum modes in a ring fiber by using multiple coherent inputs[J]. Optics Letters, 2012, 37(17): 3645-3647.
- [22] Shao W, Huang S J, Liu X P, et al. Free-space optical communication with perfect optical vortex beams multiplexing [J]. Optics Communications, 2018, 427: 545-550.
- [23] Yoshihiko A, Chen M Z, Wright E M, et al. Dynamics of a levitated microparticle in vacuum trapped by a perfect vortex beam: three-dimensional motion around a complex optical potential[J]. Journal of the Optical Society of America B, 2017, 34(6): C14-C19.
- [24] Xu H F, Zhang R, Sheng Z Q, et al. Focus shaping of partially coherent radially polarized vortex beam with tunable topological charge[J]. Optics Express, 2019, 27(17): 23959-23969.
- [25] Liu Z W, Yan S, Liu H G, et al. Superhigh-resolution recognition of optical vortex modes assisted by a deep-learning method[J]. Physical Review Letters, 2019, 123(18): 183902.
- [26] Ma H X, Li X Z, Tai Y P, et al. *In situ* measurement of the topological charge of a perfect vortex using the phase shift method[J]. Optics Letters, 2017, 42(1): 135-138.
- [27] Li X Z, Tai Y P, Lü F J, et al. Measuring the fractional topological charge of LG beams by using interference intensity analysis[J]. Optics Communications, 2015, 334: 235-239.
- [28] Pinnell J, Rodríguez-Fajardo V, Forbes A. Quantitative orbital angular momentum measurement of perfect vortex beams[J]. Optics Letters, 2019, 44(11): 2736-2739.
- [29] Zhao Y Y, Huang X T, Chang Z H, et al. Measure the arbitrary topological charge of perfect optical vortex beams by using the dynamic angular double slits[J]. Optics Express, 2021, 29(21): 32966-32972.
- [30] 刘雪莲,陈旭东,林志立,等.深度学习辅助测量强散射涡旋光束拓扑荷数[J].光学学报,2022,42(14):1426001.
Liu X L, Chen X D, Lin Z L, et al. Deep-learning-assisted detection for topological charges of vortex beams through strong scattering medium[J]. Acta Optica Sinica, 2022, 42(14):

1426001.

- [31] 马文琪, 路慧敏, 王建萍, 等. 基于空间光调制器和深度学习的涡旋光束产生[J]. 光学学报, 2021, 41(11): 1107001.
Ma W Q, Lu H M, Wang J P, et al. Vortex beam generation based on spatial light modulator and deep learning[J]. Acta Optica Sinica, 2021, 41(11): 1107001.

Optica Sinica, 2021, 41(11): 1107001.

- [32] Zhao Q, Dong M, Bai Y H, et al. Measuring high orbital angular momentum of vortex beams with an improved multipoint interferometer[J]. Photonics Research, 2020, 8(5): 745-749.

Recognition of Orbital Angular Momentum of Fractional Perfect Optical Vortex Beam Based on Convolutional Neural Network and Multiaperture Interferometer

Du Haobo, Chen Jun*, Fu Gangkun, Li Yansong, Wang Hailong, Shi Yan, Zhao Chunliu, Jin Shangzhong**

College of Optical and Electronic Technology, China Jiliang University, Hangzhou 310018, Zhejiang, China

Abstract

Objective Perfect optical vortex beams (POVBs) are widely applied in particle manipulation, optical communication, and laser material processing for the constant spot size under different topological charges (TCs). Compared with the integer-order POVB, the fractional POVB which is a dark hollow beam with an opening in the angular intensity distribution is more flexible in particle manipulation and beam shaping. In addition, the fractional POVB carries the information with fractional TC orders and has a greater communication capacity. In order to realize the above applications of the fractional POVB, the accurate recognition of the orbital angular momentum (OAM) mode is of great significance. In this paper, a method combining convolutional neural network (CNN) and multiaperture interferometer (MI) is proposed to recognize the modes of 0.01-order fractional POVB. Experimental results show that the recognition accuracy of 0.01-order fractional POVB reaches 100% under an ideal environment. Under the condition of a sector-shaped opaque obstacle of 90° and 180°, the recognition accuracy of 0.01-order fractional POVB reaches 100% and 99.5%, respectively. This study provides a new method for recognizing 0.01-order fractional POVB, which is of great significance for the application and promotion of this beam.

Methods Our method for fractional POVB recognition combines an MI and a CNN. First, the POVB to be detected is sent to the MI, and interference patterns are collected at the output of the interferometer. In this work, the MI is a seven-aperture plate that is realized through a spatial light modulator (SLM). The aperture radius r_0 equals 0.25 mm. The interference patterns have a one-to-one correspondence to the TC of the input beam. Secondly, a CNN model is trained with the interference patterns of 0.01-order fractional POVB. The network structure is shown in Fig. 3, and it is a six-layer network consisting of four convolutional blocks and two fully connected layers. The full dataset of the CNN model contains 4000 intensity images, which are labeled by 10 different TCs from $l = 8.01$ to $l = 8.10$. The intensity images of POVB are collected by a CCD. The dataset is divided into the training set, validation set, and test set according to the ratio of 7 : 2 : 1. The training set and validation set are put into the designed model in this experiment for training, while the test set is not placed into the model training but is used to test the robustness of the model. Finally, the trained model is tested by the test set. The sector-shaped opaque obstacle in a non-ideal environment is simulated by SLM. The number of collected datasets and the experimental procedure in the non-ideal environment case are the same as those in the ideal environment.

Results and Discussions Fig. 6 shows the training results and confusion matrix of 0.01-order fractional POVB after a MI under the ideal environment. In Fig. 6 (a), the solid line is the training accuracy curve, indicating that the training accuracy reaches 100% after three epochs. The dashed line is the verification accuracy curve, indicating that the verification accuracy reaches 100% after eight epochs. In Fig. 6 (b), the results of the confusion matrix show that the test accuracy is 100%. Fig. 8 (a) and Fig. 8 (b) show the training results and confusion matrix of 0.01-order fractional POVB after an MI under a sector-shaped opaque obstacle of 90°. In Fig. 8 (a), the solid line is the training accuracy curve, indicating that the training accuracy reaches 100% after three epochs. The dashed line is the verification accuracy curve, indicating that the verification accuracy reaches 100% after eight epochs. In Fig. 8 (b), the results of the confusion matrix show that the test accuracy is 100%. Fig. 8 (c) and Fig. 8 (d) show the training results and confusion matrix of 0.01-order

fractional POVB after an MI under a sector-shaped opaque obstacle of 180° . In Fig. 8 (c), the solid line is the training accuracy curve, indicating that the training accuracy reaches 100% after five epochs. The dashed line is the verification accuracy curve, indicating that the verification accuracy reaches 100% after eight epochs. In Fig. 8 (d), the results of the confusion matrix show that the test accuracy is 99.5%. According to the above results, we can prove that our method is feasible and efficient.

Conclusions In this paper, a method combing CNN with MI is proposed to accurately classify 0.01-order fractional POVB under ideal and non-ideal environments. This method utilizes the one-to-one relationship between the TC of the input beam and the intensity pattern of the interferometer and the classification ability of CNN to accurately classify the 0.01-order fractional POVB. The experimental results show that in the ideal environment, the recognition accuracy of this method for 0.01-order fractional POVB reaches 100%. For the non-ideal environments with a sector-shaped opaque obstacle of 90° and 180° , the recognition accuracy of this method for 0.01-order fractional POVB is 100% and 99.5%, respectively. The proposed method provides a new scheme for the recognition of fractional POVB. We hope that it can be helpful in the applications of fractional optical vortices.

Key words physical optics; convolutional neural network; multiaperture interferometer; fractional perfect optical vortex beam; orbital angular momentum; topological charge